

## Radar Target and Moving Clutter Separation Based on the Low-Rank Matrix Optimization

Yin, Jiapeng; Unal, Christine; Schleiss, Marc; Russchenberg, Herman

**DOI**

[10.1109/TGRS.2018.2837051](https://doi.org/10.1109/TGRS.2018.2837051)

**Publication date**

2018

**Document Version**

Final published version

**Published in**

IEEE Transactions on Geoscience and Remote Sensing

**Citation (APA)**

Yin, J., Unal, C., Schleiss, M., & Russchenberg, H. (2018). Radar Target and Moving Clutter Separation Based on the Low-Rank Matrix Optimization. *IEEE Transactions on Geoscience and Remote Sensing*, 56(8), 4765 - 4780. <https://doi.org/10.1109/TGRS.2018.2837051>

**Important note**

To cite this publication, please use the final published version (if applicable). Please check the document version above.

**Copyright**

Other than for strictly personal use, it is not permitted to download, forward or distribute the text or part of it, without the consent of the author(s) and/or copyright holder(s), unless the work is under an open content license such as Creative Commons.

**Takedown policy**

Please contact us and provide details if you believe this document breaches copyrights. We will remove access to the work immediately and investigate your claim.

# Radar Target and Moving Clutter Separation Based on the Low-Rank Matrix Optimization

Jiapeng Yin<sup>1</sup>, *Student Member, IEEE*, Christine Unal, Marc Schleiss, and Herman Russchenberg

**Abstract**—A novel algorithm is put forward to separate radar target and moving clutter based on a combination of the low-rank matrix optimization (LRMO) and the decision tree. Similar to the moving object detection in the field of automated video analysis, the proposed separation method, which is carried out in the range-Doppler domain, makes use of different motion variations of radar target and clutter in the spectrogram sequence. The technique is very general, but the focus of this paper is on narrowband moving clutter suppression in a weather radar. The first step in implementing this method is the generation of a range-Doppler spectrogram sequence. Then, the LRMO is applied to the obtained sequence to divide target and moving clutter into foreground and background. From the foreground sequence which is obtained by solving the LRMO, foreground frequency and spectral width are combined in a decision tree to obtain a filtering mask to mitigate the narrowband moving clutter and noise. Data collected by a polarimetric Doppler weather radar known as the IRCTR Drizzle Radar are used to validate the performance of the proposed algorithm. Moreover, its effectiveness in removing narrowband moving clutter is quantitatively assessed through comparisons with another clutter mitigation method.

**Index Terms**—Decision tree, low-rank matrix optimization (LRMO), narrowband moving clutter, range-Doppler spectrogram sequence, target and clutter separation, weather radar.

## I. INTRODUCTION

**R**ADAR, as an effective remote sensing platform, is designed to detect and track targets using electromagnetic waves [1]. According to different targets of interest and applications, a radar is configured with various waveforms, wavelengths, scanning strategies, and so on. Radar clutter, which is defined as an interfering radar echo from other objects [2], is a relative concept for different radar systems. For instance, air traffic control radar [3] and marine radar [4] regard vehicles (e.g., airplanes and ships) as targets and precipitation as clutter, while for weather radar [5], the opposite is the case.

Sometimes, “clutter” may also be valuable. One example is the Doppler weather surveillance radar network (WSR-88D) also known as Next Generation Radar (NEXRAD) that consists of 159 high-resolution S-band polarimetric Doppler

weather radars [6]. The primary function of NEXRAD is to detect and track precipitation and help predict the atmospheric threats to life and property. Therefore, precipitation will be the target for NEXRAD. However, using the same radar system, ornithologists can also track bird echoes and conduct studies about bird migration [7]. Hence, for multifunctional radar systems, target and clutter separation techniques may be more compelling than clutter mitigation. Indeed, with proper radar target and clutter separation, clutter mitigation is normally easily fulfilled. Another benefit of target and clutter separation is radar target feature extraction. For example, fuzzy logic algorithms, which can reach distinct decisions based on overlapping or “noise contaminated” measurements, are widely used for hydrometeor classification in a weather radar [8]. The performance of a fuzzy-logic-based classification largely depends on the hydrometeor feature extraction that is time-consuming for manual selection. Last but not least, when signal and clutter overlap, such as precipitation buried by wind turbine clutter (WTC) [9], good separation techniques are needed to retrieve the target signal. Apart from precipitation, vehicles, birds, and wind turbines, other echoes from buildings, moving sea waves, and changeable radio frequency interference (RFI) can also be sensed by a radar.

This paper focuses on a weather radar. The weather radar clutter, which significantly affects both the quality of the measurement and the observation of targets, can be divided into stationary clutter and nonstationary clutter according to their Doppler velocity. Methods of stationary clutter (e.g., ground clutter) mitigation can mainly be divided into two types, namely, the time-domain and the Doppler-domain methods. Regression filters [10] in the temporal domain and the Gaussian model adaptive processing (GMAP) [11] in the spectral domain are specifically designed to remove the clutter centered around  $0 \text{ ms}^{-1}$ . However, when these techniques are applied to radar data not contaminated by ground clutter, this will lead to a signal loss. Hence, a proper clutter detection algorithm should be implemented before clutter filtering. Recently, the Clutter Environment Analysis using Adaptive Processing (CLEAN-AP), which is based on the phase of the autocorrelation spectral density, has been proposed [12]. CLEAN-AP integrates clutter detection and filtering in one algorithm, and this filter uses both magnitude and phase for improved notch width determination that results in smaller biases. Furthermore, it has a better clutter suppression performance, and the variance of estimates is reduced [13]. However, while CLEAN-AP can deal with normal-propagation clutter and anomalous-propagation clutter, it is not a mitigation

Manuscript received August 25, 2017; revised December 15, 2017 and April 12, 2018; accepted May 11, 2018. Date of publication May 31, 2018; date of current version July 20, 2018. (*Corresponding author: Jiapeng Yin.*)

The authors are with the Department of Geoscience and Remote Sensing, Delft University of Technology, 2628 CN Delft, The Netherlands (e-mail: j.yin@tudelft.nl; c.m.h.unal@tudelft.nl; m.a.schleiss@tudelft.nl; h.w.j.russchenberg@tudelft.nl).

Color versions of one or more of the figures in this paper are available online at <http://ieeexplore.ieee.org>.

Digital Object Identifier 10.1109/TGRS.2018.2837051

0196-2892 © 2018 IEEE. Personal use is permitted, but republication/redistribution requires IEEE permission. See [http://www.ieee.org/publications\\_standards/publications/rights/index.html](http://www.ieee.org/publications_standards/publications/rights/index.html) for more information.

***Green Open Access added to TU Delft Institutional Repository***

***'You share, we take care!' – Taverne project***

**<https://www.openaccess.nl/en/you-share-we-take-care>**

Otherwise as indicated in the copyright section: the publisher is the copyright holder of this work and the author uses the Dutch legislation to make this work public.

technique for moving clutter, such as airplanes, ships, cars, or wind turbines.

Nonstationary clutter has also attracted a lot of interest in the past years. The characteristics of birds and insects are presented in [14]–[17]. Besides, [18] demonstrates the effectiveness of the image processing techniques together with the fuzzy logic algorithm to mitigate other clutter, such as sea and chaff clutter. WTC is both stationary and nonstationary. It significantly deteriorates a radar system performance because of the large-intensity backscattering from the tower and the moving blades [19]. The undesirable effect of WTC on a weather radar is illustrated in [20] and [21] on an air traffic control radar in [22] and on a marine radar in [23]. Methods, such as interpolation [24], [25], signal decomposition [9], [26], and machine learning [27], have been investigated to mitigate the WTC. Last but not least, RFI arising from the radio local area network is an increasing concern for the radar community, for example, the C-band European operational weather radar network [28]. Disturbances, such as dots, spokes, and spikes, are brought in the radar plan position indicator (PPI) by RFI that severely lowers the quality of radar data [29]. Comparably, artifacts caused by the radar system itself also affect the usage of radar data [30], [31]. Most of the time, artifacts are speckles along the whole range bins in some azimuth directions in the PPI. Moreover, these speckles are nonstationary when observed in the Doppler domain, making it impossible to mitigate them with conventional clutter suppression methods. These artifacts affect not only the reflectivity but also the Doppler and polarimetric measurements. For example, artifacts have been shown to influence the display of the polarimetric Doppler X-band radar IRCTR Drizzle Radar (IDRA) since its installation in 2007. Also, the high-resolution polarimetric Doppler X-band radar MESEWI suffers from an analogous problem [32]. So do the Bonn X-band radar systems [33]. Literature [34] puts forward a polarimetric optimization (POLO) method to remove the artifacts in the IDRA. This technique can improve the suppression of the clutter while keeping most of the precipitation. However, it cannot completely mitigate all artifacts and will lose weak signals below  $-2$  dBZ. Therefore, drizzle measurements may be suppressed.

Taking advantage of the different motion variations of radar target and clutter in the spectrogram sequence, we propose a novel algorithm to separate radar target and moving clutter based on the low-rank representation. The low-rank matrix optimization (LRMO) [35] has been successfully adopted in many applications, such as video denoising [36], keyword extraction [37], image alignment [38], and automated video analysis [39]. In addition, the low-rank representation has been used to suppress in-wall clutter for a through-the-wall radar [40]. However, it has never been used for weather radar target and moving clutter separation. The proposed technique can be used in different radar systems as long as radar target and clutter have different motion properties in the spectrogram sequence. In this paper, we apply the method to the removal of narrowband moving artifacts in a weather radar. The structure of this paper is as follows. In Section II, the details of the proposed method are provided, including the range-Doppler spectrogram sequence generation

and the LRMO method. Furthermore, the LRMO technique is applied to weather radar data in Section III. Specifically, the IDRA artifacts are introduced, the details of the technique are discussed, and a decision tree is designed to produce the filtering mask. In addition, parameters for the decision tree and the spectrogram sequence are selected. In Section IV, the performance verification is given. Section V illustrates the parameter sensitivity of spectrogram sequence, LRMO, and signal-to-noise ratio (SNR). Finally, Section VI draws the conclusions and discusses some other potential application of this technique.

## II. LOW-RANK MATRIX OPTIMIZATION IN RADAR

This section discusses the details of how to implement the proposed radar target and moving clutter separation method. The technique is mainly based on a different motion behavior of target and clutter in the range-Doppler spectrogram sequence. The rationale for using the range-Doppler spectrograms is that they integrate both range information and velocity information (including both the radial Doppler velocity and its change) that are normally different for radar target and clutter. This makes it easier to distinguish between them. However, the tradeoff is the difficulty of implementation. This is where the LRMO technique comes into play. In the framework of the LRMO, the separation between radar target and moving clutter can be represented as the problem of detecting contiguous outliers in the low-rank representation. The separation implementation will be accomplished on a range-Doppler spectrogram sequence. In this case, radar target can be seen as the foreground, while moving clutter will represent the background that has nonzero Doppler velocity but is relatively fixed at the same Doppler velocity in the spectrogram sequence. More details will be given in Section III-A.

### A. Spectrogram Sequence Generation

Suppose that the radar transmits a coherent burst of  $P$  pulses as

$$s_T(t) = \sum_{p=0}^{P-1} x(t - pT_r) \cdot e^{j2\pi f_c t} \quad (1)$$

where  $t$  is the time,  $x(t)$  is the complex envelope of one pulse,  $T_r$  is the pulse repetition interval, and  $f_c$  is the center frequency. Correspondingly, the received echo can be expressed as

$$s_R(t) = a \cdot s_T[t - \tau(t)] = a \cdot s_T \left[ t - \left( \tau_0 - \frac{2v}{c}t \right) \right] \quad (2)$$

where  $a$  is the attenuated amplitude,  $\tau(t)$  is the round-trip time delay,  $\tau_0 = (2R_0/c)$  is the initial time delay,  $R_0$  is the initial range of the target,  $c$  is the speed of light, and  $v$  is the target Doppler velocity. Substituting (1) into (2), we get

$$s_R(t) = \tilde{a} \cdot \sum_{p=0}^{P-1} x \left[ \left( 1 + \frac{2v}{c} \right) t - \tau_0 - pT_r \right] \cdot e^{j2\pi f_c \left( 1 + \frac{2v}{c} \right) t} \quad (3)$$

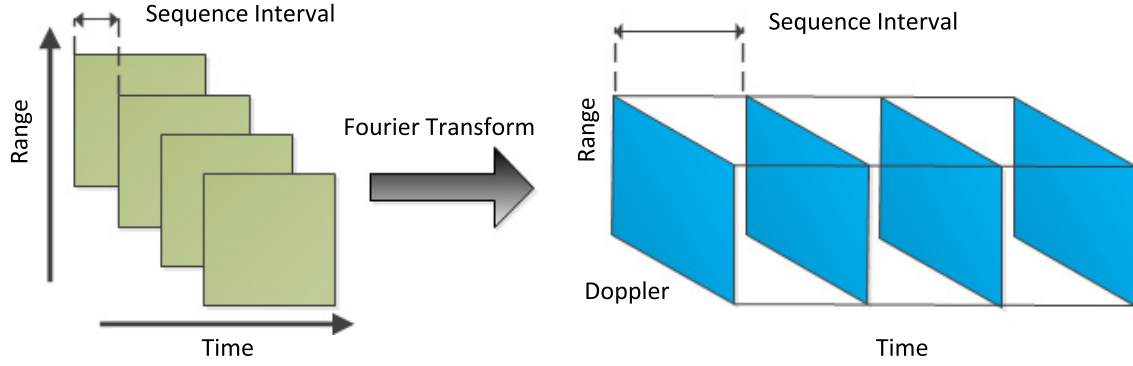


Fig. 1. Schematic of the range-Doppler spectrogram sequence generation.

where the constant phase term  $e^{-j2\pi f_c \tau_0}$  is included in the complex amplitude  $\tilde{a} = a \cdot e^{-j2\pi f_c \tau_0}$ . By introducing the fast time  $t_f = t - pT_r$  in (3) and demodulating into baseband, the signal is expressed as

$$s_R(t_f, p) = \tilde{a} \cdot x \left[ \left(1 + \frac{2v}{c}\right) t_f - \tau_0 + \frac{2v}{c} pT_r \right] \cdot e^{j2\pi f_c \frac{2v}{c} (t_f + pT_r)}. \quad (4)$$

In the radar, target velocity is assumed to be constant in one pulse duration  $T_r$ , and we have  $vT_r \ll \Delta R$ , where  $\Delta R$  is the range resolution. This means that the Doppler effect in the fast time and the contribution of  $(2v/c)t_f$  in the amplitude are negligible, thus removing the term  $(2v/c)t_f$ , and (4) can be expressed as

$$s_R(t_f, p) = \tilde{a} \cdot x \left( t_f - \tau_0 + \frac{2v}{c} pT_r \right) \cdot e^{j2\pi f_c \frac{2v}{c} pT_r}. \quad (5)$$

To simplify the derivation, replacing the discrete slow time  $pT_r$  with  $t_s$  in (5), we have

$$s_R(t_f, t_s) = \tilde{a} \cdot x \left( t_f - \tau_0 + \frac{2v}{c} t_s \right) \cdot e^{j2\pi f_c \frac{2v}{c} t_s}. \quad (6)$$

Then, applying the short-time Fourier transform (STFT) over slow time  $t_s$  in (6), we can obtain the range-Doppler spectrogram sequence as

$$X(t_f, f_d, n) = |\text{STFT}(s_R(t_f, t_s))|^2 \quad (7)$$

where  $t_f$  relates with the range bin,  $f_d$  represents the Doppler bin whose size is related to the STFT window length, and  $n$  represents the  $n$ th frame of the spectrogram sequence.

Finally, discretizing the spectrogram sequence, we obtain  $X(r, d, n) = [X_1, \dots, X_N]$ , where  $r$ ,  $d$ , and  $n$  represent the range bin, the Doppler bin, and the sequence number, respectively. If the number of range bins is  $R$ , the number of Doppler bins is  $D$ , and the sequence number is  $N$ , we have  $X \in \mathbb{R}^{Q \times N}$ , where  $Q = R \times D$ .

The above process can be visualized via the schematic in Fig. 1. Given one range-time data, we move forward and backward by an  $L$  sequence interval in the slow time to obtain  $N$  range-time data. Furthermore, by the Fourier transform,  $N$  range-Doppler spectrograms are obtained. Next, the LRMO can be used to separate radar target from moving clutter based

on the spectrogram sequence. The sequence interval  $L$  and the sequence number  $N$  are the important parameters. Their selection is discussed in more detail in Section V-A.

### B. Low-Rank Matrix Optimization

In this paper, the capital letters representing numbers are cardinal and their lowercase formats are ordinal. The low-rank matrix optimization is employed in this paper, following the same notations as in [39]. Assuming that  $X_n \in \mathbb{R}^Q$  denotes the  $n$ th frame of the range-Doppler spectrogram sequence, the  $q$ th pixel in the  $n$ th frame is denoted as  $qn$ . While  $B = [B_1, \dots, B_N] \in \mathbb{R}^{Q \times N}$  represents their corresponding background images and  $S = [S_1, \dots, S_N] \in \{0, 1\}^{Q \times N}$  is a binary matrix denoting the foreground support

$$S_{qn} = \begin{cases} 0, & \text{if } qn \text{ is background} \\ 1, & \text{if } qn \text{ is foreground.} \end{cases} \quad (8)$$

$P_S(X)$  represents the orthogonal projection of a matrix  $X$  onto the linear space of matrices supported by  $S$

$$P_S(X)(q, n) = \begin{cases} 0, & \text{if } S_{qn} = 0 \\ X_{qn}, & \text{if } S_{qn} = 1 \end{cases} \quad (9)$$

and  $P_{S^\perp}(X)$  is its complementary projection. Then, we have  $P_S(X) + P_{S^\perp}(X) = X$ .

In the spectrogram sequence, we model radar target as the foreground areas and moving clutter as the background. Background areas are relatively fixed among the produced spectrogram sequence that means that they are highly correlated with each other, forming a low-rank matrix  $B$ . This constraint on  $B$  can be expressed as

$$\text{rank}(B) \leq K \quad (10)$$

where  $K$  is a constant to be predefined.

On the other hand, the foreground areas are defined as radar targets that move differently from the background. They act as the outliers in the low-rank representation. The binary states of entries in the foreground support  $S$  can be modeled by a Markov random field [41]. Considering a graph  $G = (v, \epsilon)$ , where  $v$  is the set of vertices denoting all the pixels in the sequence and  $\epsilon$  is the set of edges connecting neighboring

pixels, and assuming that we have no additional prior knowledge about the locations of objects, the energy of  $S$  is given by the Ising model [41] as

$$\beta \sum_{qn \in \nu} S_{qn} + \gamma \sum_{(qn, pm) \in \epsilon} |S_{qn} - S_{pm}| \quad (11)$$

where  $\beta > 0$  represents the potential of  $S_{qn}$  being 0 or 1 and  $\gamma > 0$  controls the strength of dependence between  $S_{qn}$  and  $S_{pm}$ .

Finally, we consider the signal model that describes the formation of  $X$ . On the one hand, in the foreground,  $S_{qn} = 1$ ,  $X_{qn}$  equals to the foreground intensity, and  $X_{qn}$  is not constrained. On the other hand, in the background,  $S_{qn} = 0$  and  $X_{qn} = B_{qn} + \epsilon_{qn}$ , where  $\epsilon_{qn}$  denotes independent and identically distributed Gaussian noise. Thus,  $B_{qn}$  should be the best fit to  $X_{qn}$  in the least squares sense in this case.

Combining the above background, foreground, and signal models, the objective function to estimate  $B$  and  $S$  is given by

$$\begin{aligned} \min_{B, S_{qn} \in \{0, 1\}} & \frac{1}{2} \sum_{qn: S_{qn}=0} (X_{qn} - B_{qn})^2 \\ & + \beta \sum_{qn \in \nu} S_{qn} + \gamma \sum_{(qn, pm) \in \epsilon} |S_{qn} - S_{pm}| \\ \text{s.t. rank}(B) & \leq K. \end{aligned} \quad (12)$$

To make (12) tractable, the rank operator on  $B$  is relaxed with the nuclear norm [42]. Rewriting (12) in the dual form and with the matrix operators, we obtain the following problem:

$$\begin{aligned} \min_{B, S_{qn} \in \{0, 1\}} & \frac{1}{2} \|P_{S^\perp}(X - B)\|_F^2 + \alpha \|B\|_* \\ & + \beta \|S\|_1 + \gamma \|A \cdot \text{vec}(S)\|_1 \end{aligned} \quad (13)$$

where  $\|\cdot\|_F$  is the Frobenius norm,  $\|\cdot\|_*$  is the nuclear norm, and  $\|\cdot\|_1$  is the  $\ell_1$  norm.  $A$  is the node-edge incidence matrix of  $G$ , and  $\text{vec}$  means the vectorization of matrix  $S$ . The parameter  $\alpha > 0$  relates with the background low rank  $K$ . Actually, the parameters  $\alpha$ ,  $\beta$ , and  $\gamma$  are the weights of background low rank, foreground sparsity, and foreground smoothness in the LRMO. To minimize the LRMO, they should be adjusted properly.

The objective of the optimization in (13) is to estimate  $B$  and  $S$ . For details about the estimation, we refer to [39]. As for the selection of the parameters  $\alpha$ ,  $\beta$ , and  $\gamma$ , it is also well discussed in [39], and they are set to the same values in this paper. Specifically,  $\alpha$  is initialized to be the second largest singular value of  $X$  and is reduced by a factor  $1/\sqrt{2}$  until  $\text{rank}(B) > K$ . A similar procedure is followed for  $\beta$ , starting at a relatively large value and then reducing by a factor 0.5 after each iteration until  $\beta$  reaches  $4.5\sigma^2$ , where  $\sigma^2$  is the estimated noise level calculated by the variance of  $X - B$ . Overall, only two parameters, i.e.,  $K$  and  $\gamma$ , need to be chosen. The optimization algorithm is empirically configured by setting  $K = \lfloor \sqrt{N} \rfloor$  and  $\gamma = 5\beta$ , where  $\lfloor \cdot \rfloor$  means the lower integer part. The influence of  $K$  and  $\gamma$  on the LRMO performance will be discussed in Section V-B.

TABLE I  
IDRA SPECIFICATIONS [43]. THE BOLDFACE INDICATES PARAMETERS USED FOR THE OPERATIONAL MODE

Radar type	Linear FM-CW
Polarization	Fully polarimetric
Center frequency (GHz)	<b>9.475</b>
Transmitted power (W)	1, 2, 5, 10, <b>20</b>
Range resolution (m)	3, 6, 15, <b>30</b>
Scanning rate (rpm)	<b>1</b>
Sweep time ( $\mu$ s)	204.8, <b>409.6</b> , 8192.2, 1638.4, 3276.8
Frequency excursion (MHz)	<b>5</b> , 10, 20, 50
Antenna beamwidth ( $^\circ$ )	<b>1.8</b>
Elevation angle ( $^\circ$ )	<b>0.5</b>

### III. APPLICATION TO WEATHER RADAR

In this section, the proposed method will be applied to the field of the weather radar. Specifically, we will address the problem of artifacts contaminating the PPI of the polarimetric Doppler weather radar IDRA documented in [43]. The features of artifacts are first analyzed to show the necessity to separate artifacts from precipitation in the IDRA. Furthermore, the details of the LRMO applied to mitigate artifacts are discussed, including a general LRMO separation and a specific filtering mask design based on a decision tree. Finally, parameters for the decision tree and the spectrogram sequence are discussed.

#### A. Clutter Analysis

The IDRA radar continuously scans the atmosphere, and its measurements are displayed in near-real time [44]. The IDRA rotates horizontally at a speed of 1 r/min with a fixed elevation angle of  $0.5^\circ$ . The specifications of the polarimetric Doppler weather radar are shown in Table I. All the radar data recorded from April 2009 until now are freely accessible to the public on the website named 4TU.centre for Research Data [45]. These data provide a long-term observation to monitor the trends in the precipitation change. The Doppler velocity resolution corresponds to 512 samples used for Doppler processing, and in this paper, 512 samples are kept for all the processing.

The raw PPI of one radar measurement at 02:00 UTC on July 1, 2011 is shown in Fig. 2(a). Artifacts whose intensity is larger than the background noise level on the PPI are visible in some azimuths and labeled in the figure. Note that the azimuths displaying artifacts are not fixed among different PPIs. To take a closer look at the raw range-Doppler spectrogram (i.e., one ray in radar PPI), Ray 68 is extracted, as shown in Fig. 2(b). Some artifacts are visible along the whole range bins, and they have different nonzero Doppler velocities. Furthermore, range bin 300 (e.g., 9 km) is considered and its Doppler spectrum is plotted, as shown in Fig. 2(c). We can see that the power intensity of the precipitation is weaker or has the same order of magnitude as the one of artifacts and ground clutter. After integrating the whole Doppler bins, resulting in one reflectivity value, the true reflectivity of precipitation will be biased by the artifacts and ground clutter. Several methods for dealing with the ground clutter have been proposed. However, the artifacts are harder

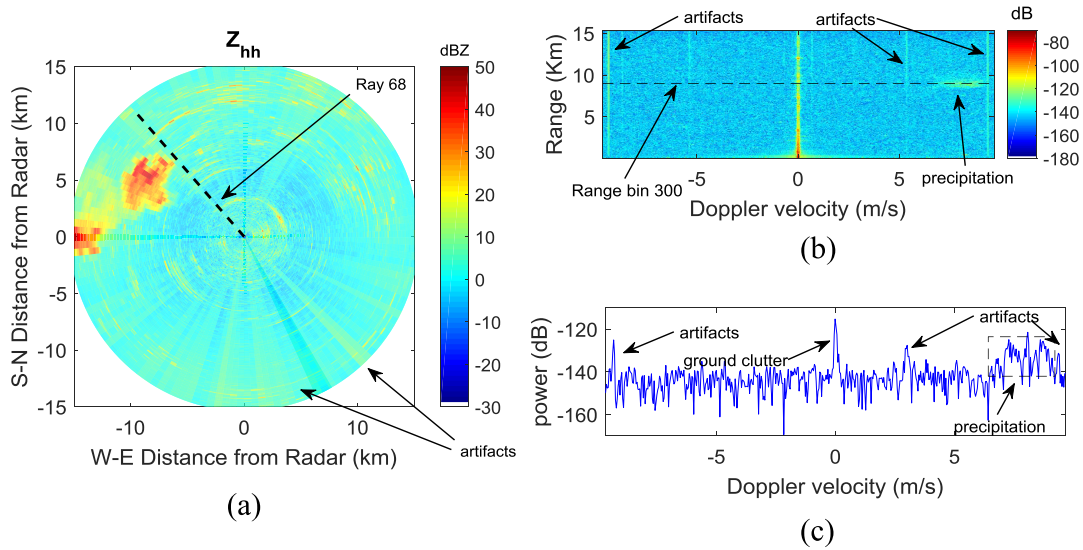


Fig. 2. Radar artifact analysis. (a) Raw PPI. (b) Raw spectrogram of Ray 68. (c) Raw Doppler spectrum of range bin 300.

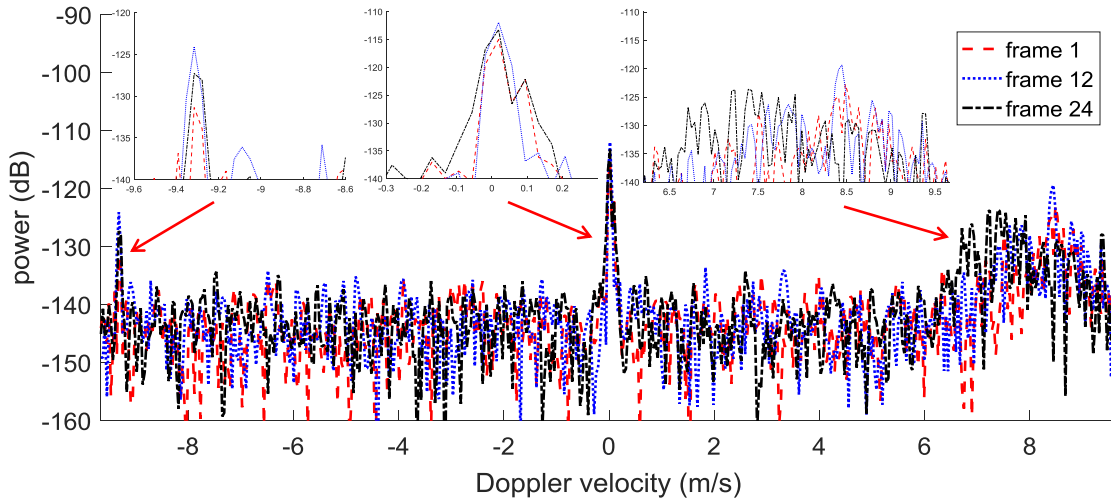


Fig. 3. Multiple spectra of the same range bin from different spectrograms.

to mitigate. The exact phenomena responsible for producing the artifacts in the radar data remain unknown at this point. As mentioned in Section I, such artifacts are not unique to the IDRA radar system. In [46], similar artifacts are observed in the range-Doppler spectrogram, and the authors attribute them to RFI. However, Cho [47] states that “in the Doppler spectral domain, Wi-Fi interference in weather radars presents as white noise.” This makes us believe that the artifacts observed in this paper may not necessarily come from RFI. Since we do not know what they are, we prefer to refer to artifacts as narrowband moving clutter due to the fact that they are narrow-band in the Doppler domain with random Doppler velocity values, however, fixed during a small amount of time. Finally, when we take Ray 68 and generate the range-Doppler spectrogram sequence according to Fig. 1, it can be observed that artifacts have the same Doppler velocity over the sequence, while precipitation Doppler velocities vary slightly. The motion variation in the spectrogram sequence will be used as a key feature for the proposed separation method.

Note that artifacts present in the IDRA data are narrow-band and their intensity is moderate. Therefore, when there is heavy precipitation with wide spectral width and large reflectivity, the impact of artifacts is negligible. Hence, artifacts (i.e., narrowband moving clutter) and precipitation separation in IDRA mentioned in this paper are mainly aimed at moderate, light precipitation, and drizzle.

### B. LRMO Applied to Artifact Removal

The LRMO technique is very general and has been successfully used in many applications. In this paper, it is specifically designed for narrowband moving clutter mitigation in the weather radar. Observed in the range-Doppler spectrogram sequence, the multiple spectra of the same range bin (Range bin 290 is taken as an example) from different spectrograms are shown in Fig. 3.

Precipitation, which has small variation in its Doppler velocity interval because the radar scans and the

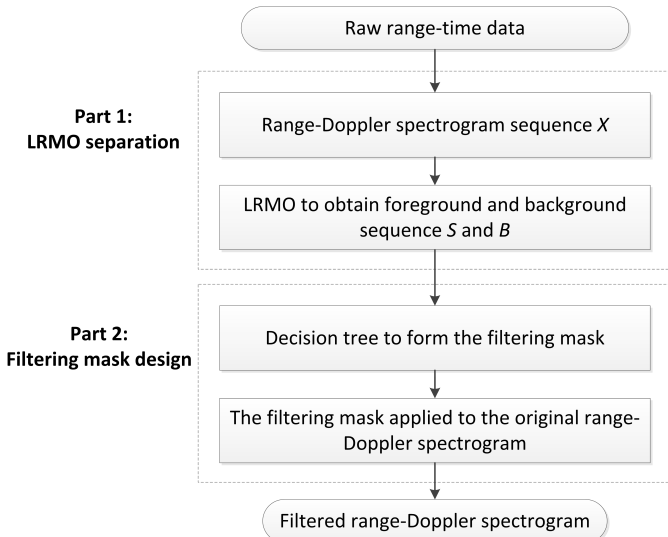


Fig. 4. Flowchart of the LRMO applied to weather radar to mitigate the narrowband moving clutter.

precipitation advects over time, can be modeled in the foreground, while artifacts, which have the same Doppler velocity over the sequence, can be modeled in the background. As for ground clutter, it will also remain in the foreground, and the reasons are related to two aspects. One is that spectrograms in the sequence are generated from different time samples (i.e., corresponding to different azimuth angles for a rotating radar), which may contain stationary targets (e.g., buildings and trees) of different spectral widths. The other is related to the spectral leakage of an frequency modulation continuous wave radar [48], especially those range bins near the radar. The ground clutter with different spectral widths forms a high-rank matrix in the spectrogram sequence, leading to its appearance in the foreground. Finally, noise will retain in the background because of the signal model provided in the first part of (12). Specifically, when  $S_{qn} = 0$ ,  $(1/2) \sum_{qn: S_{qn}=0} (X_{qn} - B_{qn})^2$  should be minimized, and thus, noise will be built into background. In addition, the values of parameter  $\beta$  and  $\gamma$  are adaptively obtained and they are positively related to the estimated noise level. When the estimated noise level is larger, namely smaller SNR, to minimize (13), more data will be built into the background, which may lead to some precipitation loss. More discussion of the impact of SNR will be given in Section V-C.

The flowchart that consists of the LRMO separation (i.e., the general part) and the filtering mask design (i.e., the specific part) is shown in Fig. 4. First, the input of this technique is the raw range-time data. Then, in Part 1, the range-Doppler spectrogram sequence  $X$  is generated according to Fig. 1. Note that the spectrogram sequence expressed in dB scale should be normalized in the interval of  $[0, 255]$ . Such normalization will improve the performance of the algorithm. Next, the foreground sequence  $S$  and background sequence  $B$  can be separated using the LRMO.

In Part 2, a filtering mask based on a decision tree is applied to remove the narrowband moving clutter and noise in the weather radar. The details of the decision tree will be discussed

next. The filtering mask can be applied to the raw spectrogram obtained from the raw range-time data by the Fourier transform to select the precipitation and mitigate the narrowband moving clutter. The detailed parameter determination will be discussed in Section III-D.

### C. Filtering Mask Design

After the application of the LRMO, most of the precipitation should be in the foreground. However, sometimes, there may be observations wrongly attributed into the foreground (thereafter refer to as excess background). Therefore, we design a decision tree to detect those observations. Once the excess background has been identified, a filtering mask is applied to the raw spectrogram (i.e.,  $X_{N/2}$ ) to select the precipitation part. Note that ground clutter will also be kept in the filtering mask, but it can be mitigated later with another technique.

The filtering mask design is given by a decision tree shown in Fig. 5. The input of the decision tree is the foreground frequency and the spectral width, both of which are derived from the foreground sequence  $S$  after the LRMO. The foreground frequency, defined as the sum of the foreground sequence, is positively related to the probability of precipitating areas. The spectral width helps to recognize the precipitation that is the distributed target in the view of the weather radar, and thus, its spectral width should be distributed along a moderate number of Doppler bins. The excess background will be categorized by a large spectral width and small-to-moderate foreground frequency or small spectral width and small foreground frequency. Finally, a filtered foreground is obtained, which acts as a filtering mask on the raw spectrogram. Next, the details of the decision tree will be discussed. We start with the input, namely, the foreground frequency and the spectral width. The foreground frequency  $F$  is defined as the sum of the foreground sequence  $S$

$$F(r, d) = \sum_{i=1}^N S_i(r, d) \quad (14)$$

where  $r \in [1, R]$  and  $d \in [1, D]$  represent the range bin and Doppler bin, respectively. The larger the values of the foreground frequency are, the more likely the area contains precipitation. Based on the foreground frequency  $F$ , the mask index  $M$  that indicates precipitation or ground clutter can be obtained

$$M(r, d) = \begin{cases} 0, & F(r, d) = 0 \\ 1, & F(r, d) \neq 0. \end{cases} \quad (15)$$

Furthermore, by adding up the mask index  $M$  along its Doppler axis, the spectral width  $W$  in each range bin is obtained

$$W(r) = \sum_{d=1}^D M(r, d). \quad (16)$$

A proper threshold  $T_1$  should be set to make a comparison with the calculated maximum  $W$  that is expressed as  $W_{\max}$  to further check the existence of excess background. If  $W_{\max} > T_1$ , it means that excess background may be

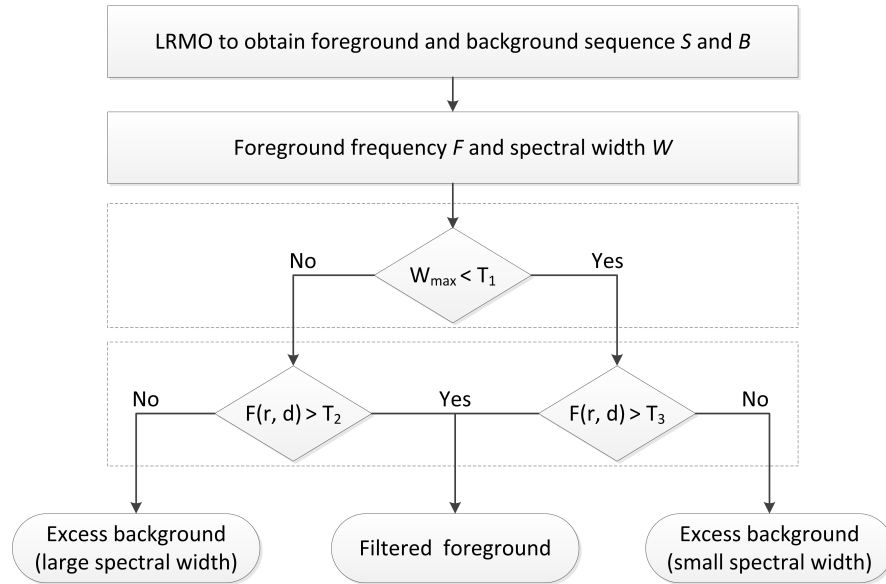


Fig. 5. Decision tree to form a filtering mask for the raw range-Doppler spectrogram.

TABLE II  
PRECIPITATION CASES USED TO ANALYZE THE SPECTRAL WIDTH

Case No	Date & Time	Rain Type
1	2011-07-01 02:00	moderate
2	2011-07-01 12:00	moderate
3	2014-08-22 13:00	moderate
4	2016-01-15 12:00	light

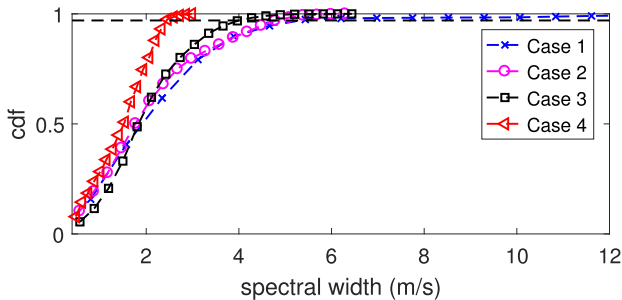


Fig. 6. Cumulative distribution function of precipitation spectral width.

present. However, with the different environments (e.g., wind) and radar configurations (e.g., antenna scanning strategy), it will result in a different Doppler broadening that finally influences the observed spectral width of precipitation  $W^{\text{prec}}$ . Hence, it is more reliable to study the real radar measurements to estimate the threshold  $T_1$  that is defined as

$$T_1 = \max(W^{\text{prec}}) \quad (17)$$

where  $\max(\cdot)$  means the maximum value. Such estimations are done by using radar data in Section III-D.

The spectral width  $W$  can help to detect the existence of excess background. Then, the way to mitigate the excess background should also be explored. One way to do this is to use the foreground frequency  $F$ . Typically, the mask index  $M$  in (15) indicates the precipitation areas, which should be used as the filtering mask. On the one hand, if there is excess background with a large spectral width in the foreground,

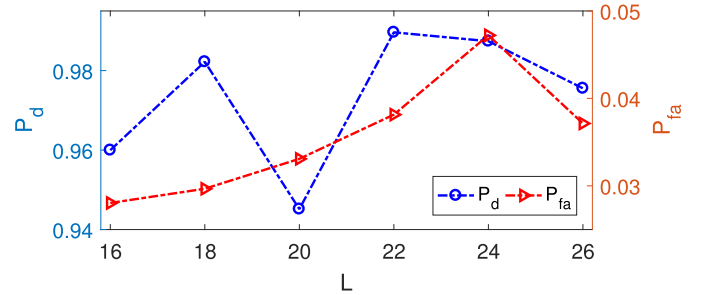


Fig. 7. Detection probability of precipitation and background with different sequence intervals.

all the precipitation should be selected in the foreground sequence. Then, if the corresponding  $F$  is larger than one large-value threshold  $T_2$ , the mask index  $M$  can be kept as the filtering mask. Otherwise, the mask index  $M$  should be excluded. On the other hand, if there is no excess background with a large spectral width in the foreground, all the mask indexes related to  $M = 1$  should be kept as the final filtering mask. Thus, we set the corresponding  $F$  larger than one small-value threshold  $T_3$  to further remove the excess background with a small spectral width.

In summary, the detection and mitigation of excess background in the foreground, as well as the filtering mask generation, can be visualized as a decision tree shown in Fig. 5. If  $W_{\max} > T_1$ , it means that the background separation is not sufficient. In this case, all the precipitation will remain in the foreground sequence  $S$ , which means that the foreground frequency indicating precipitation is large. Next, if  $F(r, d) > T_2$ , the corresponding  $M(r, d)$  indicates precipitation. Otherwise, it is excess background with a large spectral width. On the other hand, if  $W_{\max} < T_1$ , we should keep all nonzero areas in  $F$  but add one extra condition  $F(r, d) > T_3$ , where  $T_3$  is a small value, to further remove the excess background with a small spectral width.

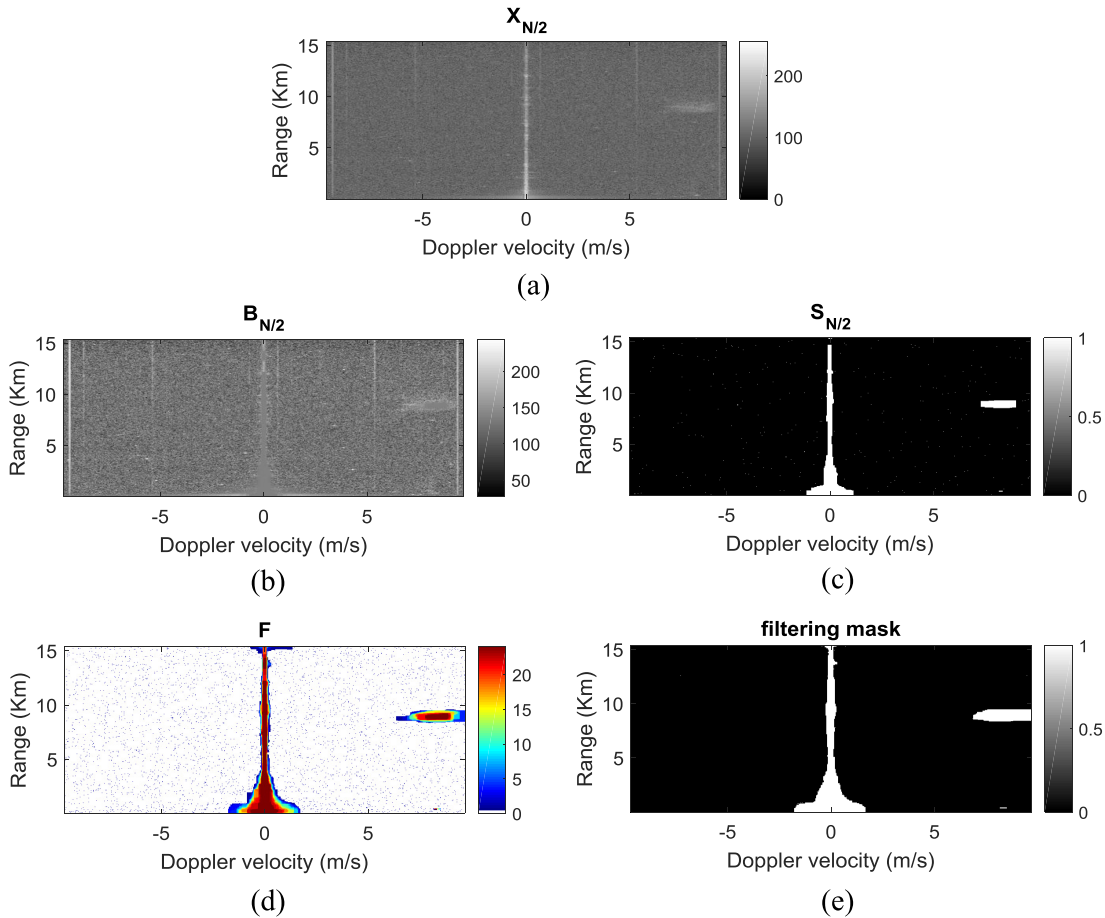


Fig. 8. Background and foreground extraction based on the LRMO. (a) Raw spectrogram  $X_{N/2}$  scaled in  $[0, 255]$ . (b) Low-rank background  $B_{N/2}$ . (c) Foreground  $S_{N/2}$ . (d) Foreground frequency  $F$ . (e) Filtering mask.

#### D. Parameter Selection

The basis of the proposed narrowband moving clutter removal method is the spectrogram sequence originating from one range-time data set. In this section, the choices of the sequence number  $N$  and sequence interval  $L$  are discussed. With  $K = \lfloor \sqrt{N} \rfloor$  in the LRMO [39], the selection of the sequence number  $N$  relates with the low-rank property of the background. Normally,  $K$  can be predefined after several target and clutter separation scenario studies, and then, the value interval of  $N$  can be given. Because calculation time increases with  $N$ , the smallest possible value should be selected. However, if  $N$  is too small, the precipitation change in the spectrogram sequence may be very small, making it difficult to put the precipitation in the foreground in the LRMO. On the contrary, when  $N$  is too large, the background may not be easy to detect as it changes too much, leading to excess background appearing in the foreground. As for the sequence interval  $L$ , it determines the correlation between the neighboring spectrograms. If  $L$  is set too large, the correlation of artifacts between the neighboring spectrograms is too small, making it impossible to model the artifacts as the low-rank matrix in the background. On the other hand, if the sequence interval is too small, the precipitation in the

foreground between the neighboring spectrograms is almost the same, meaning that it will end up in the background. Hence, the values of  $N$  and  $L$  should be well balanced. Moreover, they should meet the principle that the detection probability of precipitation  $P_d$  in the filtering mask should be close to 1 and artifacts and excess background  $P_{fa}$  (i.e., false alarm rate) in the filtering mask as low as possible.  $P_d$  is defined as the area of the precipitation in the filtering mask divided by that of the true precipitation, and  $P_{fa}$  is defined as the area of the background in the filtering mask divided by that of the true background. Note that the true area of precipitation and background is obtained by manual selection.  $P_{fa}$  quantifies the excess background in the foreground, and its removal can be done following the decision tree as discussed in Section III-C.

The sequence number  $N$  and the sequence interval  $L$  are chosen based on the IDRA data. A sensitivity analysis of  $N$  and  $L$  will be given in Section V-A. To calculate the detection probability in the filtering mask, the thresholds  $T_1$ ,  $T_2$ , and  $T_3$  in Fig. 5 should first be estimated. According to (17),  $T_1$  should be selected based on the radar data. Aiming at suppressing artifacts in the moderate, light precipitation, and drizzle, four cases of IDRA data collected during 2011–2016 are selected, as shown in Table II. The relation between the spectral width

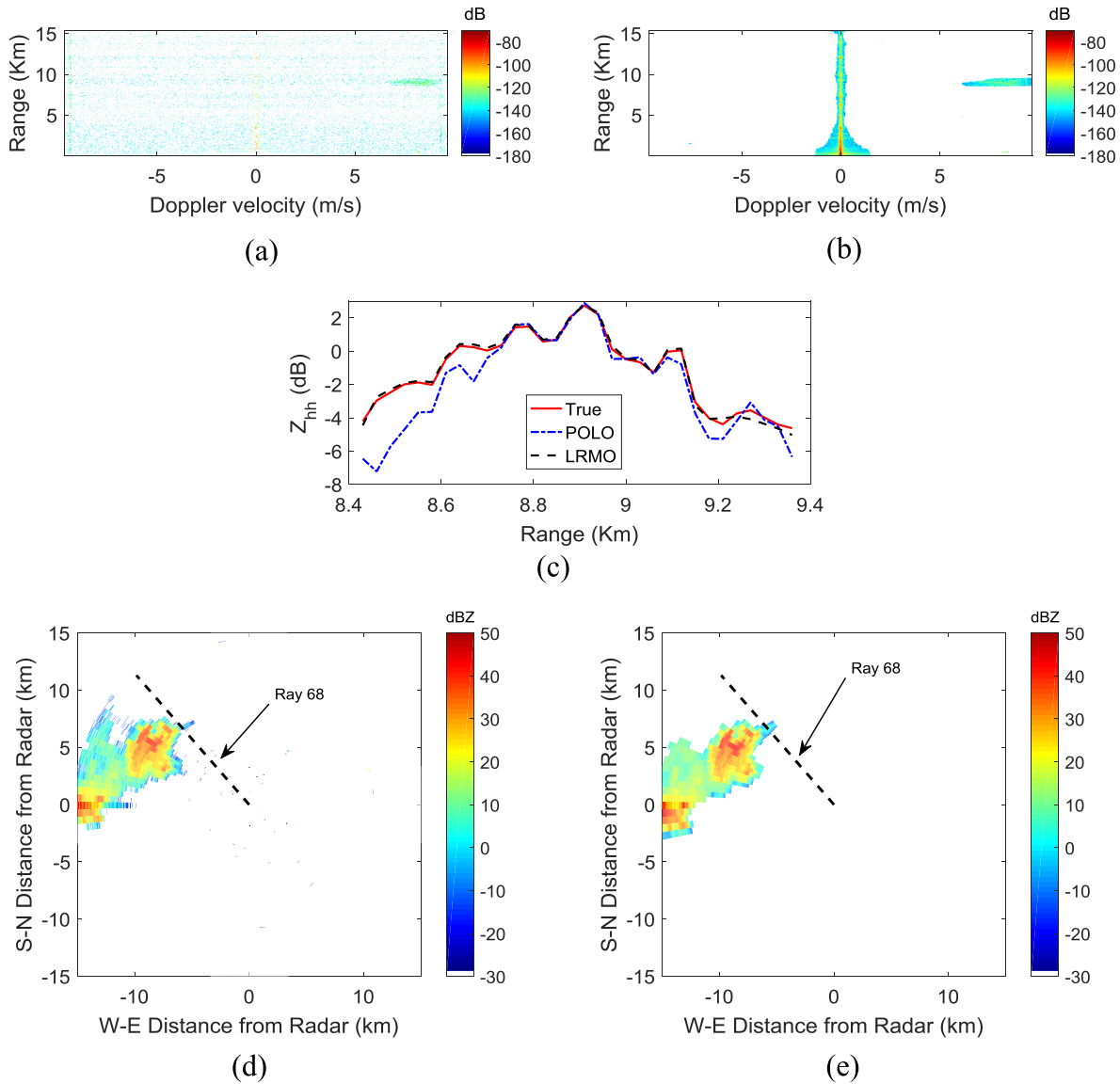


Fig. 9. Performance comparison between the POLO and LRMO. Data measured at 02:00 UTC on July 1, 2011. (a) Spectrogram after the POLO. (b) Spectrogram after the LRMO. (c) Reflectivity quantitative comparison. (d) Reflectivity PPI after the POLO. (e) Reflectivity PPI after the LRMO.

and cumulative distribution functions is shown in Fig. 6. The black dashed line is 0.97, and it indicates that almost all the spectral widths are within  $5.5 \text{ ms}^{-1}$ , which corresponds to 146 Doppler bins for the operational IDRA configuration (the Doppler velocity resolution is  $3.8 \text{ cm s}^{-1}$ ). Considering the coexistence of the ground clutter, the threshold can be set to  $T_1 = 160$ . The thresholds  $T_2$  and  $T_3$  are chosen to remove the background appearing in the foreground. As it is also discussed in Section III-C,  $T_2$  should be large, while  $T_3$  should be small. The spectrogram sequence  $N$  is obtained by moving the raw data forward and backward equally in the slow time. Hence, in the case of excess background with a large spectral width in the foreground sequence,  $T_2 = N/2$  can be set to eliminate the excess background adjacent to the precipitation in  $X_{N/2}$ . As for the excess background with a small spectral width, it appears randomly in the spectrogram sequence. Therefore, the removal can be done by setting  $T_3 = 2$  for the IDRA

measurements. Note that the noise is eliminated with the thresholding of  $T_2$  and  $T_3$ .

After the choice of the thresholds in the decision tree, the sequence number  $N$  and the sequence interval  $L$  can be selected through the detection probability and the false alarm rate in the filtering mask. After the statistical analysis of 10 cases (each case contains more than 140 rays) during the time from 2011 to 2016, the sequence number was empirically set to  $N = 24$ , which correspondingly predefines  $K = 4$ . More discussion of the  $N$  selection will be given later. The selection of the sequence interval  $L$  should fulfill the following condition: the detection probability of precipitation  $P_d$  is close to 1 and the false alarm rate  $P_{fa}$  is as low as possible. Setting  $L$  in the interval of [16, 26], we used Ray 68 of IDRA data measured at 02:00 UTC on July 1, 2011 to calculate  $P_d$  and  $P_{fa}$  that are shown in Fig. 7. Normally, with the increase in the sequence interval  $L$ , which will decrease the correlation

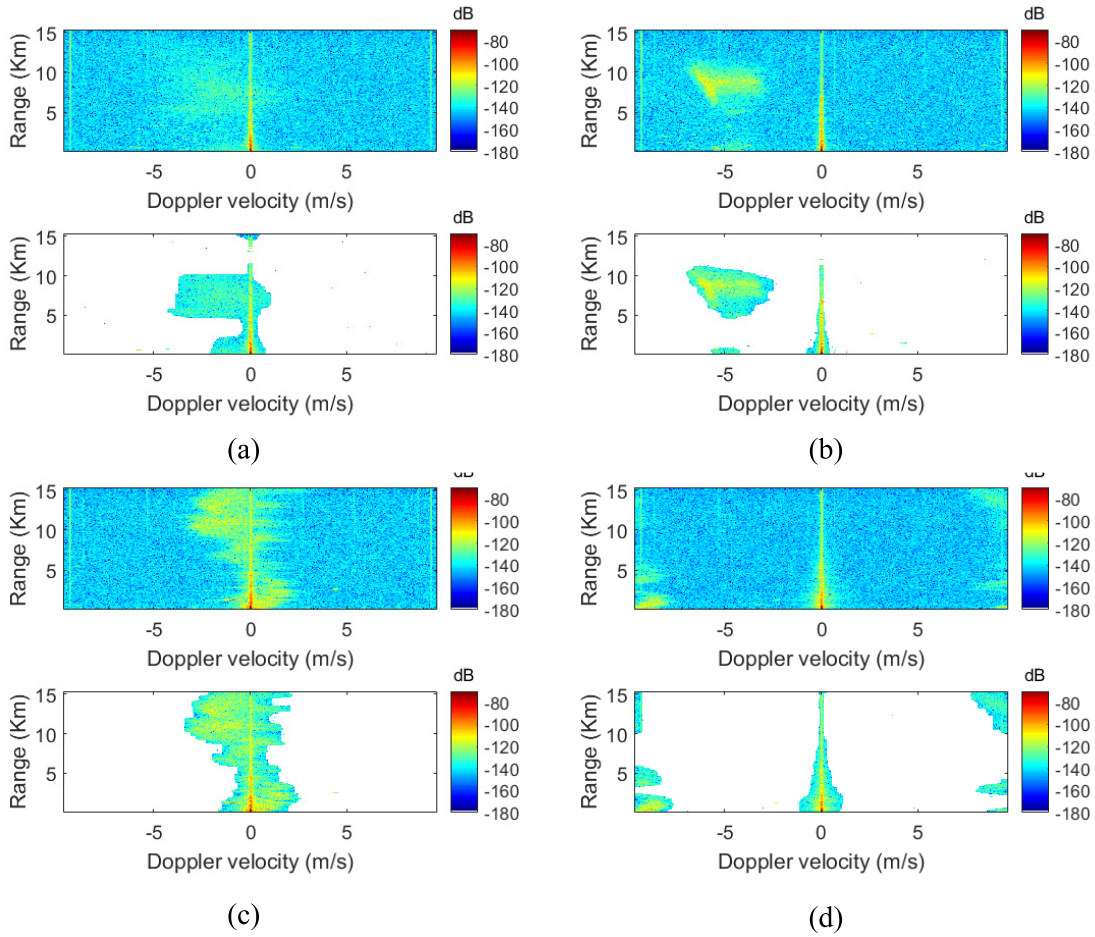


Fig. 10. Performance verification with two other cases. (a) Ray 41 and (b) Ray 61 are from 18:00 UTC on July 5, 2012. (c) Ray 51 and (d) Ray 70 are from 13:00 UTC on August 22, 2014.

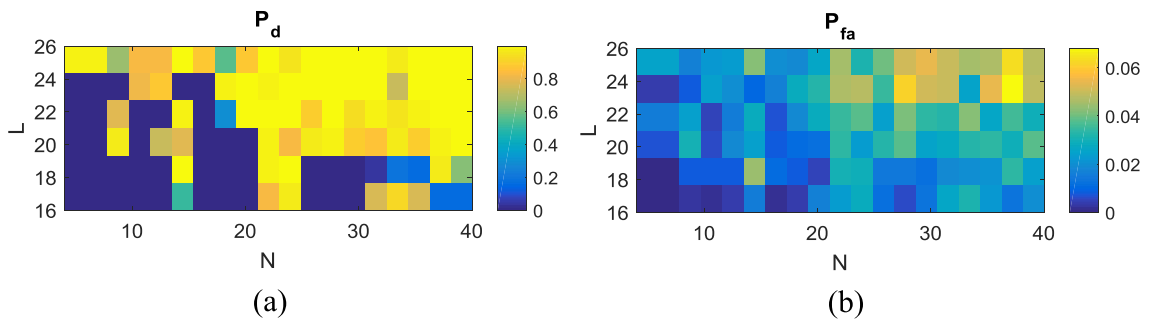


Fig. 11. Parameter selection for the spectrogram sequence. (a) Detection probability  $P_d$ . (b) False alarm rate  $P_{fa}$ .

between neighboring spectrograms,  $P_d$  and  $P_{fa}$  should also increase. This is observed when  $L \in [16, 24]$ . However, this is not true for  $L = 26$ . The reason is that the larger sequence interval  $L$  will reduce the foreground frequency  $F$ , meaning that the decrease in  $P_d$  and  $P_{fa}$  is due to the decision tree mitigation. Based on the result in Fig. 7, the deviation of  $P_d$  and  $P_{fa}$  obtained from a different  $L$  selection is not too large, which means that it should be possible to use the same value of  $L$  for other data. Finally, we choose the sequence interval  $L = 22$  that gives a good detection probability of precipitation  $P_d$  even though  $P_{fa}$  is not optimal. Indeed,

$P_{fa}$  can be further mitigated by the decision tree, which leads to acceptable values.

#### IV. PERFORMANCE VERIFICATION

The IDRA data are used to verify the performance of the proposed precipitation and narrowband moving clutter separation method. First, we check the extracted foreground and background for a given range-time data set. Ray 68 at 02:00 UTC on July 1, 2011 is used to define the raw range-Doppler spectrogram  $X_{N/2}$  in Fig. 2(b). Then, the raw spectrogram expressed in dB scale is normalized in the interval

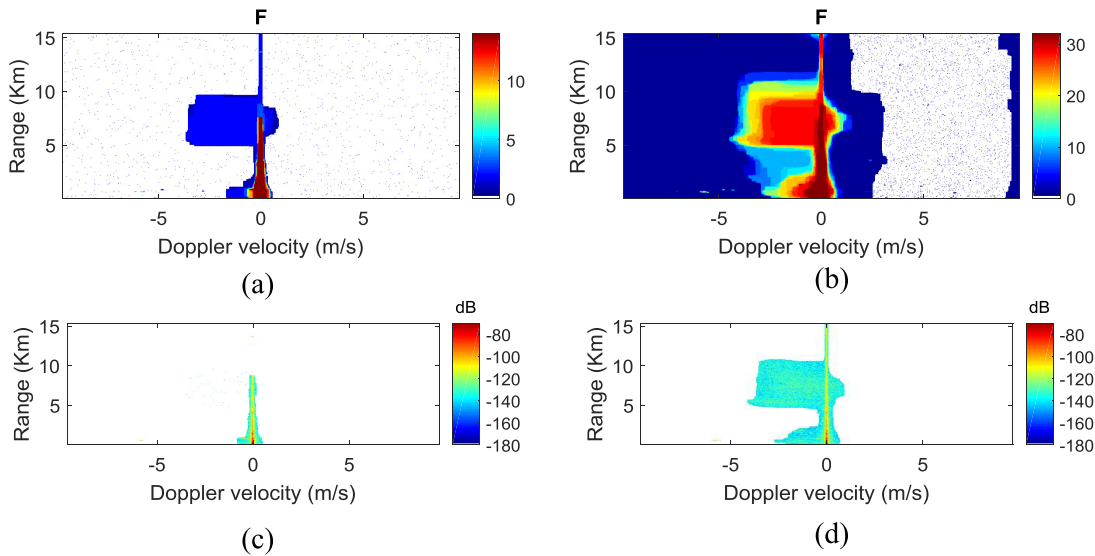


Fig. 12. Parameter selection for the spectrogram sequence. (a)  $F$  with  $N = 14$  and  $L = 22$ . (b)  $F$  with  $N = 34$  and  $L = 22$ . (c) Filtered spectrogram with  $N = 14$  and  $L = 22$ . (d) Filtered spectrogram with  $N = 34$  and  $L = 22$ .

of  $[0, 255]$ , as shown in Fig. 8(a). The corresponding low-rank background  $B_{N/2}$  and the foreground  $S_{N/2}$ , as shown in Fig. 8(b) and (c), are extracted by performing the LRMO in (13). We can observe that all the artifacts remain in the background areas, while the precipitation and the ground clutter are in the foreground areas, which is consistent with the analysis in Section III-B. However, there is some signal loss at the boundaries of the precipitating areas that corresponds to regions with a lower SNR. These areas can be recovered by using the foreground frequency  $F$  displayed in Fig. 8(d). With the considered data, the decision tree generates the filtering mask with the condition  $W_{\max} < T_1$  and  $F(r, d) > T_3$ , as shown in Fig. 8(e). Finally, the filtering mask can be applied to the raw spectrogram to mitigate the artifacts and noise. Note that the LRMO is carried out using MATLAB 2016b in a Window 7 desktop PC with a 3.6-GHz Intel Xeon E5-1620 CPU and 16-GB RAM, and the time elapsed for this separation is 69 s, which currently may be difficult to implement in real time for operational weather radar, but it could be significantly reduced using the dedicated software.

In addition, the proposed method is compared with the POLO method described in [34]. As shown in Fig. 9(a) and (b), there are some artifacts remaining in the POLO method, while the LRMO can mitigate all of them. Apart from this, the LRMO has a better performance in noise removal. There is excess background in the filtered spectrogram based on the POLO. Moreover, there is some signal loss at the boundaries of the precipitating areas, while the LRMO can avoid this problem by using more data during the processing, that is,  $N$  spectrograms instead of one for the POLO. In addition, the LRMO does not require the polarimetric measurements, making it broadly applicable.

The quantitative performance of the two methods is compared using the true reflectivity in the 8.4–9.4-km range.

The results are shown in Fig. 9(c). Legend “True” refers to the true values of reflectivity, which are manually selected. The maximum deviation between the POLO-based  $Z_{hh}$  and the true  $Z_{hh}$  is 4.2 dB, while that between the LRMO  $Z_{hh}$  and the true  $Z_{hh}$  is 0.5 dB. Both reflectivity deviations are calculated based on the assumption that the ground clutter can be completely mitigated by another technique. Note that the true  $Z_{hh}$  is around  $-2$  dBZ, corresponding to weak precipitation. This shows that the proposed LRMO technique is particularly promising for weak signal preservation.

Apart from the spectrogram comparison, the PPI assessment is also necessary. The results are shown in Fig. 9(d) and (e). Note that the PPIs are obtained by using the notch filter centered around  $0 \text{ ms}^{-1}$  to completely remove the ground clutter. The LRMO filtered PPI tends to have larger reflectivity values than the POLO ones. This is because of the better performance in weak precipitation preservation for the LRMO approach. In addition, the PPI contains 146 rays, and the PPI output also conforms the robustness of the chosen parameters for precipitation and narrowband moving clutter separation.

Finally, the performance of the proposed separation technique can also be verified by other data measured of different times, as shown in Fig. 10. Note that the parameter selection for the LRMO separation approach applied to these measurements is the same as in the study case, Ray 68 (measured at 02:00 UTC on July 1, 2011). Here, Ray 41 and Ray 61 from 18:00 UTC on July 5, 2012 and Ray 51 and Ray 70 from 13:00 UTC on August 22, 2014 are considered. From Fig. 10, we can see that the proposed artifact removal method is effective for both weak small-scale and moderate large-scale precipitation with different velocities ranging from  $0 \text{ ms}^{-1}$  to the maximum unambiguous Doppler velocity. Note that the very weak precipitation areas in Fig. 10(a) are also successfully extracted by the proposed technique.

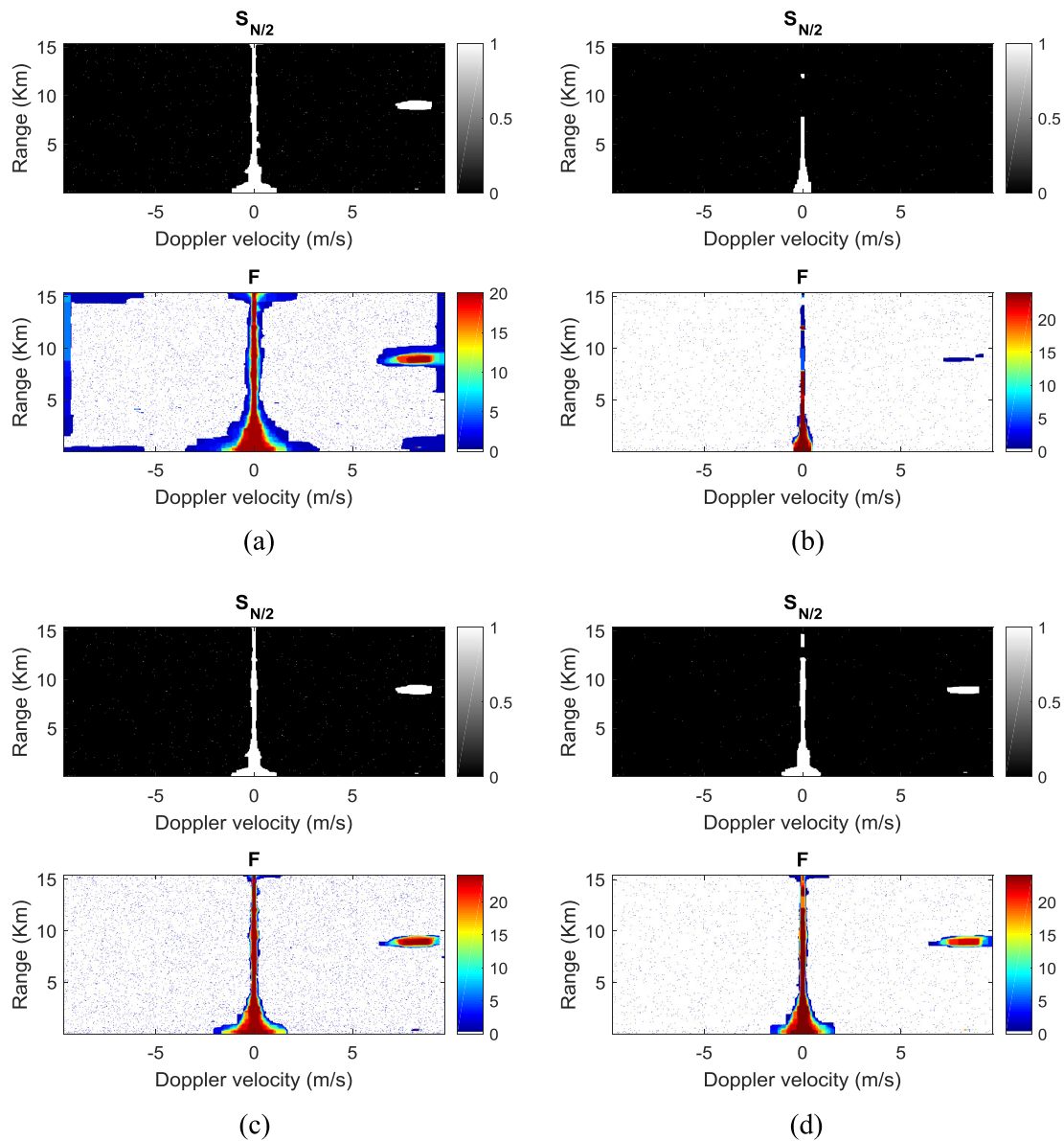


Fig. 13. Parameter selection for the LRMO. (a)  $K = 3$  and  $\gamma = 5\beta$ . (b)  $K = 5$  and  $\gamma = 5\beta$ . (c)  $K = 4$  and  $\gamma = 4\beta$ . (d)  $K = 4$  and  $\gamma = 6\beta$ .

## V. PARAMETER SENSITIVITY ANALYSIS

### A. Spectrogram Sequence Parameter Selection

To explore the influence of  $N$  and  $L$ , a simulation was conducted by setting  $N$  in the interval of  $[4, 40]$  in a step of 2 and  $L$  in the interval of  $[16, 26]$  with the same step. This was done for Ray 68 of IDRA data measured at 02:00 UTC on July 1, 2011. Then, the detection probability  $P_d$  and the false alarm rate  $P_{fa}$  were calculated with different combinations of  $N$  and  $L$ . The results are shown in Fig. 11.

As stated in Section III-D, the selection of  $N$  and  $L$  should meet the requirement that  $P_d$  is close to 1, while  $P_{fa}$  is as low as possible. From Fig. 11, it can be observed that  $P_d$  and  $P_{fa}$  tend to increase with larger values of  $N$  and  $L$ . However, when  $N$  and  $L$  are too large (i.e.,  $N > 24$  and  $L > 22$ ), the increase in  $P_{fa}$  will be dominant, while  $P_d$  is already close to 1, which means that most of the precipitation is in the foreground and more excess background is appearing. On the other hand,

when  $N$  and  $L$  are smaller than 20,  $P_d$  is relatively small, except when  $N = 14$  for which we get some promising  $P_d$ . However, this may be a local optimum specific to the used data. Therefore, we decided to use  $N = 24$  and  $L = 22$ .

Next, we made a comparison between different values of  $N$  for a fixed value of  $L = 22$ . From Fig. 11, we conclude that fixing  $L = 22$ , with  $N = 14$ ,  $N = 24$ , and  $N = 34$ , leads to similar  $P_d$  and  $P_{fa}$  values. Taking another case, namely, Ray 41 of the measurement at 18:00 UTC on July 5, 2012 shown in Fig. 10(a), we applied the LRMO with parameter setting  $N = 14$ ,  $N = 24$ , and  $N = 34$ . Note that the ray used in this experiment is related to very weak precipitation. The corresponding filtered spectrograms are shown in Figs. 10(a) and 12(c) and (d), respectively. In addition, the results of  $F$  with different parameter sets are shown in Fig. 12. The computation time depends nonlinearly on  $N$ , so the smaller  $N$  is, the faster the LRMO will be performed. In this case, the elapsed time for different  $N$  values is 41, 115,

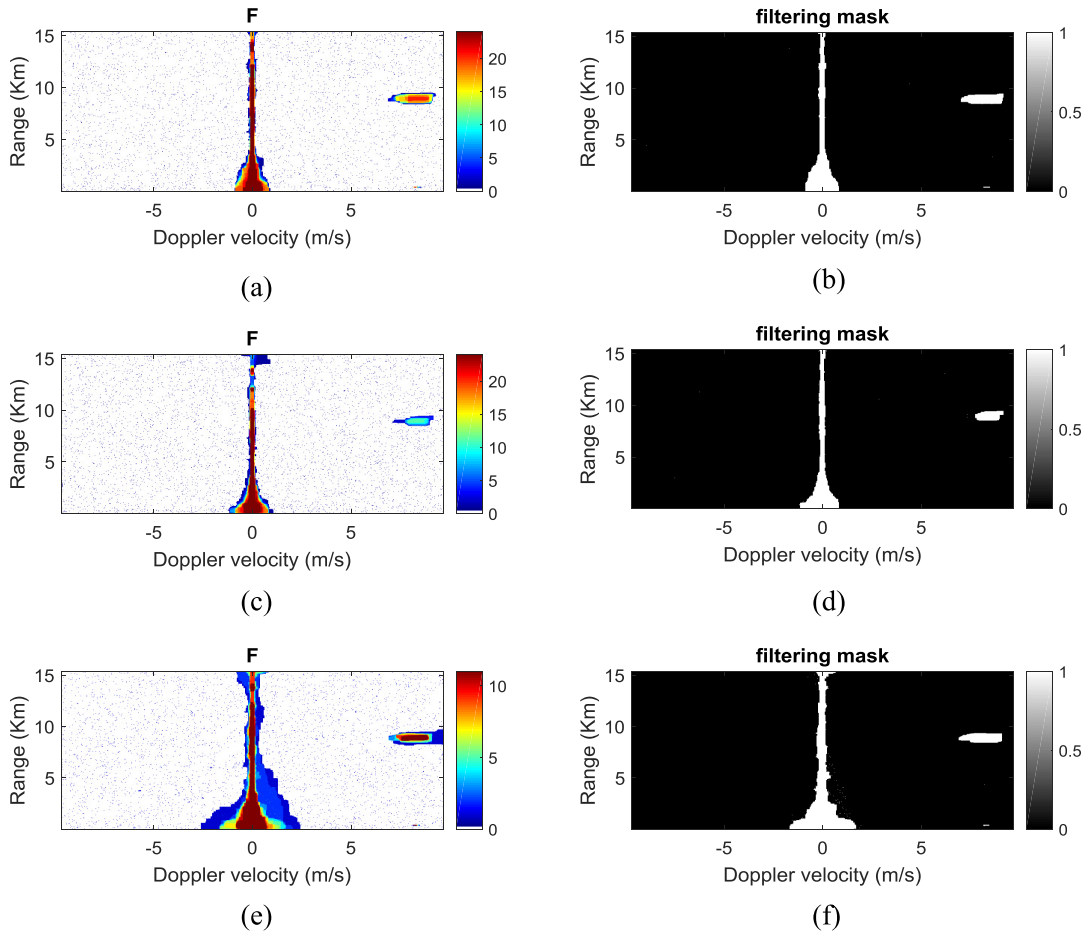


Fig. 14. Different SNRs for the LRMO. (a)  $F$  with  $K = 4$  and noise floor 10 dBW. (b) Filtering mask with  $K = 4$  and noise floor 10 dBW. (c)  $F$  with  $K = 4$  and noise floor 20 dBW. (d) Filtering mask with  $K = 4$  and noise floor 20 dBW. (e)  $F$  with  $K = 3$  and noise floor 20 dBW. (f) Filtering mask with  $K = 3$  and noise floor 20 dBW.

and 133 s. However, as stated in Section III-D,  $N$  should not be too small, and otherwise, it is difficult to put the precipitation in the foreground, as shown in Fig. 12(a) and (c). On the other hand, when  $N$  is large, more background will appear in the foreground, because the background is no longer fixed for a long spectrogram sequence, as shown in Fig. 12(b) and (d).

In summary, both the sequence number  $N$  and the sequence interval  $L$  should be well balanced. When applying this technique to other radar signal and clutter scenarios, the detection probability and the false alarm rate can be used to select the best combination.

### B. LRMO Parameter Selection

As stated in Section II-B, the parameter tuning for the LRMO consists of the selection of  $K$  and  $\gamma$ , since  $\alpha$  and  $\beta$  can be dynamically adjusted during the calculation procedure. Coming back to Ray 68 measured at 02:00 UTC on July 1, 2011, the sensitivity of the results with respect to the choice of  $K$  and  $\gamma$  selection is discussed. By default,  $K$  and  $\gamma$  are set to 4 (i.e.,  $\lfloor \sqrt{N} \rfloor$ ) and  $5\beta$ , respectively. First, we fix  $\gamma = 5\beta$  and change  $K$  which takes the values 3 and 5, then,  $K$  is fixed to 4, and  $\gamma$  takes the values  $4\beta$  and  $6\beta$ . The results of the corresponding  $S_{N/2}$  and  $F$  are displayed in Fig. 13.

We first explore the influence of  $K$  on the LRMO performance by fixing  $\gamma = 5\beta$ . By making a comparison with the results of the default setting as shown in Fig. 8(c) and (d), we observe that when  $K$  is too small, there is less precipitation in the background (the one with lower SNR). However, this comes at the cost of more excess background (in that case noise) in the foreground. Hence, more details can be preserved as observed in the  $F$  of Fig. 13(a). Note that in this case, it is still possible to achieve a good clutter filtering performance with larger  $F$  thresholding, which shows the flexibility in parameter selection for the proposed technique. On the other hand, when  $K$  is larger, more precipitation will end up in the background, disappearing from  $S_{N/2}$  and  $F$  as shown in Fig. 13(b). From the above analysis, we can conclude that the LRMO performance is sensitive to the selection of  $K$ . When  $K = 4$  and  $\gamma$  changes from  $4\beta$  to  $6\beta$ , there is only a slight decrease of the extent of the precipitating areas and excess background in  $S_{N/2}$  and  $F$ , as shown in Fig. 13(c) and (d). This is because  $\gamma$  controls the smoothness of the foreground, which means that the increase in  $\gamma$  will inevitably reduce the excess background and the size of the precipitating areas in the optimization. From the above analysis, it is concluded that the LRMO performance is not too sensitive to the selection of  $\gamma$ .

In summary, the LRMO performance is sensitive to the background low-rank  $K$  but not too much to the foreground smoothness  $\gamma$ . This means that the parameter  $K$  should be well predefined. Normally, we can start with the default setting, and then,  $K$  is tuned around  $\lfloor \sqrt{N} \rfloor$  until a satisfactory result is obtained. Finally,  $\gamma$  can be tuned to further improve the results.

### C. Impact of SNR

To explore the impact of SNR on the proposed technique, we simulated the signals by adding different noise levels to the original IQ data. The data used are also Ray 68 of IDRA measurements collected at 02:00 UTC on July 1, 2011. The simulated noise levels are 10 and 20 dBW, and the corresponding  $F$  and filtering mask are displayed in Fig. 14(a)–(d). Comparing with the situation without additional noise as shown in Fig. 8(d) and (e), as the intensity of the noise increases, we see that more and more weak precipitation is removed from the foreground. The reason has been explained in Section III-B, namely that with the decrease in SNR, more data will be built into background due to the optimization equation, leading to some precipitation loss. This undesired outcome can be avoided by proper parameter tuning in the LRMO, for example, by setting the value of  $K$  to 3 instead of  $K = 4$  as shown in Fig. 14(e) and (f). For the same noise level (i.e., 20 dBW), when  $K$  changes from 4 [see Fig. 14(d)] to 3 [see Fig. 14(f)], the lower  $K$  retains more precipitation in the foreground, demonstrating that a large part of the precipitation can still be recovered with this technique, even for lower SNRs.

## VI. CONCLUSION

A novel radar target and moving clutter separation technique based on a combination of the LRMO and a decision tree has been proposed. The technique is primarily based on a different motion variation of target and clutter in the range-Doppler spectrogram sequence. The technique is very general, but the focus of this paper is on narrowband moving clutter suppression in the weather radar. Although the LRMO has been widely used in many applications, this is the first application for weather radar clutter mitigation. The first step of this algorithm is the range-Doppler spectrogram sequence generation that consists of the selection of the sequence interval and the sequence number. The LRMO is then applied to the sequence to separate precipitation and moving clutter into foreground and background. An additional decision tree based on the foreground frequency and spectral width is designed to generate a filtering mask to keep precipitation and remove clutter and noise. Several precipitation cases measured by the radar IDRA are used to assess the proposed radar target and clutter separation method.

The proposed technique has several advantages. It is a good mitigation technique for narrowband moving clutter and noise, and it can also preserve weak signals. In addition, it fully takes advantage of motion properties of radar target and clutter. However, there are also some limitations. First, the performance is sensitive to the predefined low-rank value  $K$ ,

which requires proper parameter tuning. Second, it is not a complete mitigation method. In the case of IDRA, the ground clutter remains in the final filtered spectrogram, which means that another filtering method (e.g., GMAP) is necessary to fully remove all the unwanted echoes. To prevent signal loss, ground clutter detection algorithms (e.g., CMD [49]) should be implemented before ground clutter filtering. Since the presence of moving clutter may bias the ground clutter detection accuracy, we recommend to first mitigate the moving clutter and then the ground clutter. Finally, the proposed algorithm is computationally expensive, and for now, it cannot be implemented in real time for operational radar systems. However, this could be feasible using the optimized dedicated software.

It is foreseeable that the LRMO method could be extended to the WTC mitigation in the weather radar or to other radar systems such as air traffic control radar and marine radar if target and clutter have a different motion variation. In other scenarios, the decision trees can be adapted to mitigate other forms of clutter. For example, in the case of WTC mitigation in the weather radar, WTC may be attributed to the category of excess background with a large spectral width. Because WTC has a large spectral width, but small foreground frequency due to the fast-changing Doppler velocity. Furthermore, the separation technique may also be extended to include different clutter echoes in various background layers [50], with the interested target in the foreground. More research can be done in these directions in the future.

### ACKNOWLEDGMENT

The authors would like to thank W. Zhang for his discussion on the topic of the low-rank matrix optimization and J. Li and F. Uysal for their discussion on radar signal processing. They would also like to thank the anonymous reviewers for their constructive reviews, which helped to improve this paper. J. Yin would like to thank the China Scholarship Council for supporting his study at the Delft University of Technology, Delft, The Netherlands.

### REFERENCES

- [1] M. I. Skolnik, *Radar Handbook*, 3rd ed. New York, NY, USA: McGraw-Hill, 1970.
- [2] J. Eaves and E. Reedy, *Principles of Modern Radar*. New York, NY, USA: Springer, 2012.
- [3] M. S. Nolan, *Fundamentals of Air Traffic Control*. Boston, MA, USA: Cengage Learning, 2010.
- [4] J. N. Briggs, *Target Detection by Marine Radar*. Edison, NJ, USA: IET, 2004.
- [5] V. N. Bringi and V. Chandrasekar, *Polarimetric Doppler Weather Radar: Principles and Applications*. Cambridge, U.K.: Cambridge Univ. Press, 2001.
- [6] T. D. Crum and R. L. Alberty, "The WSR-88D and the WSR-88D operational support facility," *Bull. Amer. Meteorol. Soc.*, vol. 74, no. 9, pp. 1669–1687, Sep. 1993.
- [7] P. M. Stepanian, K. G. Horton, V. M. Melnikov, D. S. Zrnić, and S. A. Gauthreaux, Jr., "Dual-polarization radar products for biological applications," *Ecosphere*, vol. 7, no. 11, p. e01539, Nov. 2016.
- [8] H. Liu and V. Chandrasekar, "Classification of hydrometeors based on polarimetric radar measurements: Development of fuzzy logic and neuro-fuzzy systems, and *in situ* verification," *J. Atmos. Ocean. Technol.*, vol. 17, no. 2, pp. 140–164, Feb. 2000.

- [9] F. Uysal, I. Selesnick, and B. M. Isom, "Mitigation of wind turbine clutter for weather radar by signal separation," *IEEE Trans. Geosci. Remote Sens.*, vol. 54, no. 5, pp. 2925–2934, May 2016.
- [10] S. M. Torres and D. S. Zrnic, "Ground clutter canceling with a regression filter," *J. Atmos. Ocean. Technol.*, vol. 16, no. 10, pp. 1364–1372, Oct. 1999.
- [11] A. Siggia and R. Passarelli, Jr, "Gaussian model adaptive processing (GMAP) for improved ground clutter cancellation and moment calculation," in *Proc. Eur. Conf. Radar Meteorol. (ERAD)*, vol. 2, 2004, pp. 421–424.
- [12] D. A. Warde and S. M. Torres, "The autocorrelation spectral density for Doppler-weather-radar signal analysis," *IEEE Trans. Geosci. Remote Sens.*, vol. 52, no. 1, pp. 508–518, Jan. 2014.
- [13] S. Torres, D. Warde, and D. Zrnic, "Signal design and processing techniques for WSR-88D ambiguity resolution: Part 15 the CLEAN-AP filter," Nat. Severe Storms Lab., Norman, OK, USA, Tech. Rep., 2012, p. 69.
- [14] P. M. Stepanian and K. G. Horton, "Extracting migrant flight orientation profiles using polarimetric radar," *IEEE Trans. Geosci. Remote Sens.*, vol. 53, no. 12, pp. 6518–6528, Dec. 2015.
- [15] D. S. Zrnic and A. V. Ryzhkov, "Observations of insects and birds with a polarimetric radar," *IEEE Trans. Geosci. Remote Sens.*, vol. 36, no. 2, pp. 661–668, Mar. 1998.
- [16] V. Melnikov, M. Leskinen, and J. Koistinen, "Doppler velocities at orthogonal polarizations in radar echoes from insects and birds," *IEEE Geosci. Remote Sens. Lett.*, vol. 11, no. 3, pp. 592–596, Mar. 2014.
- [17] V. M. Melnikov, M. J. Istok, and J. K. Westbrook, "Asymmetric radar echo patterns from insects," *J. Atmos. Ocean. Technol.*, vol. 32, no. 4, pp. 659–674, 2015.
- [18] L. Alku, D. Moisseev, T. Aittomäki, and V. Chandrasekar, "Identification and suppression of nonmeteorological echoes using spectral polarimetric processing," *IEEE Trans. Geosci. Remote Sens.*, vol. 53, no. 7, pp. 3628–3638, Jul. 2015.
- [19] J. Yin, O. Krasnov, C. Unal, S. Medagli, and H. Russchenberg, "Spectral polarimetric features analysis of wind turbine clutter in weather radar," in *Proc. 11th Eur. Conf. Antennas Propag. (EUCAP)*, Mar. 2017, pp. 3351–3355.
- [20] B. M. Isom *et al.*, "Detailed observations of wind turbine clutter with scanning weather radars," *J. Atmos. Ocean. Technol.*, vol. 26, no. 5, pp. 894–910, May 2009.
- [21] L. Norin and G. Haase, "Doppler weather radars and wind turbines," in *Doppler Radar Observations-Weather Radar, Wind Profiler, Ionospheric Radar, and Other Advanced Applications*. Rijeka, Croatia: InTech, 2012.
- [22] D. Webster, "The effects of wind turbine farms on ATC radar," AWC/WAD/72/665/TRIALS, Air Warfare Center, Waddington, U.K., Tech. Rep., May 2005, p. 48.
- [23] L. S. Rashid and A. K. Brown, "Impact modelling of wind farms on marine navigational radar," in *Proc. IET Int. Conf. Radar Syst.*, Oct. 2007, pp. 1–5.
- [24] F. Kong, Y. Zhang, and R. Palmer, "Wind turbine clutter mitigation for weather radar by adaptive spectrum processing," in *Proc. IEEE Radar Conf. (RADAR)*, May 2012, pp. 0471–0474.
- [25] F. Nai, S. Torres, and R. Palmer, "On the mitigation of wind turbine clutter for weather radars using range-Doppler spectral processing," *IET Radar, Sonar Navigat.*, vol. 7, no. 2, pp. 178–190, Feb. 2013.
- [26] F. Uysal, I. Selesnick, U. Pillai, and B. Himed, "Dynamic clutter mitigation using sparse optimization," *IEEE Aerosp. Electron. Syst. Mag.*, vol. 29, no. 7, pp. 37–49, Jul. 2014.
- [27] R. Nepal, J. Cai, and Z. Yan, "Micro-Doppler radar signature identification within wind turbine clutter based on short-CPI airborne radar observations," *IET Radar, Sonar Navigat.*, vol. 9, no. 9, pp. 1268–1275, Dec. 2015.
- [28] A. Huuskonen, E. Saltikoff, and I. Holleman, "The operational weather radar network in Europe," *Bull. Amer. Meteorol. Soc.*, vol. 95, no. 6, pp. 897–907, Jun. 2014.
- [29] E. Saltikoff *et al.*, "The threat to weather radars by wireless technology," *Bull. Amer. Meteorol. Soc.*, vol. 97, no. 7, pp. 1159–1167, 2016.
- [30] J. Yin, C. M. H. Unal, and H. W. J. Russchenberg, "Narrow-band clutter mitigation in spectral polarimetric weather radar," *IEEE Geosci. Remote Sens.*, vol. 55, no. 8, pp. 4655–4667, Aug. 2017.
- [31] J. Yin, C. Unal, and H. Russchenberg, "Object-orientated filter design in spectral polarimetric weather radar," *IEEE Geosci. Remote Sens.*, to be published.
- [32] O. A. Krasnov and A. G. Yarovoy, "Polarimetric micro-Doppler characterization of wind turbines," in *Proc. 10th Eur. Conf. Antennas Propag. (EuCAP)*, Apr. 2016, pp. 1–5.
- [33] (Nov. 2017). *X-Band Radar of Bonn University*. [Online]. Available: <https://www.meteo.uni-bonn.de/messdaten/radarbilder/aktuelle-bilder-1/bonn/ppi>
- [34] J. Yin, C. Unal, and H. Russchenberg, "Polarimetric optimization for clutter suppression in spectral polarimetric weather radar," in *Proc. Eur. Radar Conf. (EuRAD)*, Oct. 2016, pp. 205–208.
- [35] G. Liu, Z. Lin, S. Yan, J. Sun, Y. Yu, and Y. Ma, "Robust recovery of subspace structures by low-rank representation," *IEEE Trans. Pattern Anal. Mach. Intell.*, vol. 35, no. 1, pp. 171–184, Jan. 2013.
- [36] H. Ji, C. Liu, Z. Shen, and Y. Xu, "Robust video denoising using low rank matrix completion," in *Proc. Conf. Comput. Vis. Pattern Recognit. (CVPR)*, Jun. 2010, pp. 1791–1798.
- [37] K. Min, Z. Zhang, J. Wright, and Y. Ma, "Decomposing background topics from keywords by principal component pursuit," in *Proc. 19th ACM Int. Conf. Inf. Knowl. Manag.*, 2010, pp. 269–278.
- [38] Y. Peng, A. Ganesh, J. Wright, W. Xu, and Y. Ma, "RASL: Robust alignment by sparse and low-rank decomposition for linearly correlated images," *IEEE Trans. Pattern Anal. Mach. Intell.*, vol. 34, no. 11, pp. 2233–2246, Nov. 2012.
- [39] X. Zhou, C. Yang, and W. Yu, "Moving object detection by detecting contiguous outliers in the low-rank representation," *IEEE Trans. Pattern Anal. Mach. Intell.*, vol. 35, no. 3, pp. 597–610, Mar. 2013.
- [40] Y. Zhang and T. Xia, "In-wall clutter suppression based on low-rank and sparse representation for through-the-wall radar," *IEEE Geosci. Remote Sens. Lett.*, vol. 13, no. 5, pp. 671–675, May 2016.
- [41] S. Z. Li, *Markov Random Field Modeling in Image Analysis*. London, U.K.: Springer-Verlag, 2009.
- [42] B. Recht, M. Fazel, and P. A. Parrilo, "Guaranteed minimum-rank solutions of linear matrix equations via nuclear norm minimization," *SIAM Rev.*, vol. 52, no. 3, pp. 471–501, 2010.
- [43] J. Figueras i Ventura, "Design of a high resolution X-band Doppler polarimetric weather radar," Ph.D. dissertation, Delft Univ. Technol., Delft, The Netherlands, 2009.
- [44] (May 2017). *Near-Real Time Reflectivity Measurements of IDRA*. [Online]. Available: <http://ftp.tudelft.nl/TUdelft/irctr-rse/idra/index.html>
- [45] (Dec. 2017). *IDRA Data Website*. [Online]. Available: <http://data.4tu.nl/repository/collection:cabauw>
- [46] C. S. Morse, R. K. Goodrich, and L. B. Corrman, "The NIMA method for improved moment estimation from Doppler spectra," *J. Atmos. Ocean. Technol.*, vol. 19, no. 3, pp. 274–295, 2002.
- [47] J. Y. N. Cho, "A new radio frequency interference filter for weather radars," *J. Atmos. Ocean. Technol.*, vol. 34, no. 7, pp. 1393–1406, 2017.
- [48] A. Melzer, A. Onic, F. Starzer, and M. Huemer, "Short-range leakage cancellation in FMCW radar transceivers using an artificial on-chip target," *IEEE J. Sel. Topics Signal Process.*, vol. 9, no. 8, pp. 1650–1660, Dec. 2015.
- [49] J. C. Hubbert, M. Dixon, and S. M. Ellis, "Weather radar ground clutter. Part II: Real-time identification and filtering," *J. Atmos. Ocean. Technol.*, vol. 26, no. 7, pp. 1181–1197, Jul. 2009.
- [50] C. Stauffer and W. E. L. Grimson, "Adaptive background mixture models for real-time tracking," in *Proc. IEEE Comput. Soc. Conf. Comput. Vis. Pattern Recognit.*, vol. 2, Jun. 1999, pp. 246–252.



**Jiapeng Yin** (S'16) received the B.S. degree in information engineering from the National University of Defense Technology, Changsha, China, in 2012. He is currently pursuing the Ph.D. degree with the Department of Geoscience and Remote Sensing, Delft University of Technology, Delft, The Netherlands.

His research interests include weather radar clutter suppression and weather radar calibration.



**Christine Unal** received the master's degree in physics from the University of Nice Sophia Antipolis, Nice, France, in 1986, and the D.E.A. degree in physics for remote sensing from the University of Paris, Paris, France, in 1987.

In 1988, she joined the Delft University of Technology, Delft, The Netherlands, where she is currently a Research Scientist. She was with the International Research Centre for Telecommunications and Radar, Delft. Since 2012, she has been with the Department of Geoscience and Remote

Sensing, Climate Institute, Delft. She has started to focus on radar polarimetric calibration and radar spectral polarimetry (quasi-simultaneous Doppler spectra of polarimetric measurements, their processing, and their interpretation). Since 2003, she has been applying this expertise to enhance the processing of atmospheric echoes. Her research interests include weather/atmospheric radar signal processing and searching for new retrieval techniques to estimate microphysical and dynamical properties of precipitation using ground-based radars.



**Herman Russchenberg** is currently the Director of the Climate Institute, Delft University of Technology, Delft, The Netherlands, where he is also the Head of the Department of Geoscience and Remote Sensing. He is also one of the leading scientists of the Cabauw Experimental Site for Atmospheric Research, Lopik, The Netherlands. He is a specialist in remote sensing of clouds and precipitation with ground-based radar, lidar, and microwave radiometry. He is experienced in theoretical and experimental research of the scattering process and the retrieval

of geophysical parameters from radar and lidar measurements.



**Marc Schleiss** received the M.Sc. degree in applied mathematics and the Ph.D. degree in environmental engineering with a focus on the space-time variability of raindrop size distributions from the Ecole Polytechnique Fédérale de Lausanne, Lausanne, Switzerland, in 2008 and 2012, respectively.

He held a post-doctoral position at the Hydrometeorology Group, Princeton University, Princeton, NJ, USA, for three years. He is currently an Assistant Professor with the Geoscience and Remote Sensing Department, Delft University of Technology, Delft,

The Netherlands. His research interests include the measurement, modeling, and prediction of precipitation based on *in situ* observations and remote sensing techniques, such as weather radar, satellites, and telecommunication links, the statistical modeling and prediction of heavy localized convective storms, and understanding how climate change affects the frequency, intensity, structure, and dynamics of hydroclimatic extremes across the globe.